



Contents lists available at ScienceDirect

Journal of Biomechanics

journal homepage: www.elsevier.com/locate/jbiomech
www.JBiomech.com

Computational analysis of glenohumeral joint growth and morphology following a brachial plexus birth injury

Nikhil N. Dixit, Daniel C. McFarland, Katherine R. Saul*

Department of Mechanical and Aerospace Engineering, North Carolina State University, Raleigh, NC, United States



ARTICLE INFO

Article history:
Accepted 21 January 2019

Keywords:

Brachial plexus birth injury
Finite element analysis
Musculoskeletal modeling
Contractures
Bone deformation

ABSTRACT

Children affected with brachial plexus birth injury (BPBI) undergo muscle paralysis. About 33% of affected children experience permanent osseous deformities of the glenohumeral joint. Recent evidence suggests that some cases experience restricted muscle longitudinal growth in addition to paralysis and reduced range of motion at the shoulder and elbow. It is unknown whether altered loading due to paralysis, muscle growth restriction and contracture, or static loading due to disuse is the primary driver of joint deformity after BPBI. This study uses a computational framework integrating finite element analysis and musculoskeletal modeling to examine the mechanical factors contributing to changes in bone growth and morphometry following BPBI. Simulations of 8 weeks of glenohumeral growth in a rat model of BPBI predicted that static loading of the joint is primarily responsible for joint deformation consistent with experimental measures of bone morphology, whereas dynamic loads resulted in normal bone growth. Under dynamic loading, glenoid version angle (GVA), glenoid inclination angle (GIA), and glenoid radius of curvature (GRC) (-1.3° , 38.2° , 2.5 mm respectively) were similar to the baseline values (-1.8° , -38° , 2.1 mm respectively). In the static case with unrestricted muscle growth, these measures increased in magnitude (5.2° , -48° , 3.5 mm respectively). More severe joint deformations were observed in GIA and GRC when muscle growth was restricted (GVA: 3.6° , GIA: -55° , GRC: 4.0 mm). Predicted morphology was consistent with literature reports of *in vivo* glenoid morphology following postganglionic BPBI. This growth model provides a framework for understanding the most influential mechanical factors driving glenohumeral deformity following BPBI.

© 2019 Elsevier Ltd. All rights reserved.

1. Introduction

BPBI is the most common nerve injury among children (Foad et al., 2008), affecting 0.4–4 per 1000 newborns (Cheng et al., 2015). It primarily occurs due to neck hyperextension during a difficult childbirth, resulting in nerve root avulsion or rupture of the plexus; C5–C6 roots of the brachial plexus are most commonly damaged, affecting the shoulder and elbow flexion function (Al-Qattan, 2003). Abnormal growth patterns of the glenoid and humeral head are frequent sequelae of BPBI, observed in humans (Kozin, 2004; Pearl and Edgerton, 1998) as well as in a rat model of BPBI employing neurectomy (Crouch et al., 2015). Retroversion, declination, and flattening of the glenoid (Brochard et al., 2016; Hogendoorn et al., 2010) with flattened and smaller humeral heads (Sibinski et al., 2010; Kozin, 2004) are most typical.

The mechanical environment of the developing glenohumeral joint following BPBI is altered due to reduced limb use associated with muscle paralysis, restricted range of motion, and restricted muscle growth. Individuals affected with BPBI experience postural deformities, including an internally rotated and adducted arm with restricted range of motion (ROM) (Kozin, 2004). The restriction in ROM leads to disuse of the arm and a static shoulder (Sheehan et al., 2014). Recent evidence from rodent models of BPBI suggests that the severe contractures associated with BPBI may be a result of restricted longitudinal growth of affected muscles. Restricted growth of the biceps brachii was observed only after a postganglionic injury (injury distal to the dorsal root ganglion) with corresponding restriction of elbow ROM, whereas there was no observed length difference in a preganglionic injury, and no contracture reported (Nikolaou et al., 2015). Therefore, it is possible that static loading of the paralyzed shoulder and altered loading from disrupted muscle growth may play independent roles after BPBI.

It is known that bone development is greatly affected by its environment with both biological stimuli and the mechanical

* Corresponding author at: North Carolina State University, 911 Oval Drive, Campus Box 7910, Raleigh, NC 27695-7910, United States.
E-mail address: ksaul@ncsu.edu (K.R. Saul).

environment (Shefelbine and Carter, 2004) playing pivotal roles in bone morphology (Heegaard et al., 1999). For example, biological growth for long bones is proportional to the cellular activity, whereas mechanical environment modulates growth in proportion to the stress state, with static loads hindering and dynamic loads promoting bone growth (Giorgi et al., 2014). Clinical reports suggest that the mechanical loading of the shoulder in BPBI may be an important driver of bone deformity. For example, glenoid deformity is reported to be positively correlated to shoulder contracture (Al-Qattan, 2003). Further, in the case of nerve root avulsion, with injury proximal to the nerve root ganglion, patients typically have muscle weakness or paralysis without severe contractures or bone deformity (Pearl and Edgerton, 1998; Kozin, 2004; Bhardwaj et al., 2013). Prior biomechanical analyses using a computational musculoskeletal model of BPBI revealed that restriction of muscle growth would result in glenohumeral loading that is more compressive and posteriorly directed compared to an unimpaired limb, consistent with observed glenoid changes (Crouch et al., 2014; Cheng et al., 2015). However, this study did not consider the effects of static loading on the growth of bone following injury, nor did it directly link altered loading to the magnitude of morphological change.

It is unclear whether altered mechanical loading is sufficient to explain glenoid morphology after BPBI, and whether static loading or restricted muscle growth is the primary driver of changes. Therefore, our goal was to develop a computational simulation method and evaluate its feasibility to capture the effects of static loading and paralysis with and without restricted muscle growth on developing glenohumeral joint morphology after BPBI.

2. Methods

We used an iterative computational framework (Fig. 1) to analyze the influence of altered loading on bone morphology following BPBI. The overall approach was to estimate joint loads under 3

clinically-relevant conditions using a musculoskeletal modeling platform (OpenSim 3.3, Stanford University) and apply these loads in a finite element analysis (Abaqus 6.13.3, Dassault Systemes) to predict bone growth in response to biological and mechanical stimuli. Specifically, we simulated three conditions to examine the effects of reduced motion of the shoulder and restricted muscle growth: 1) dynamic loading (intact shoulder); 2) static with unrestricted muscle growth; 3) and static with restricted muscle growth. This analysis was applied to the geometry of a neonatal rat shoulder, derived from an existing rat model of BPBI for which quantitative descriptions of bone deformities are available (Li et al., 2010; Crouch et al., 2015); rat and human shoulder anatomy are known to be similar (Norlin et al., 1994). We simulated the growth of the humerus and scapula over 8 weeks of rat growth (equivalent to 5.8 human years) (Crouch et al., 2015) from a baseline undeformed initial condition representing 0 days postnatal.

2.1. Finite element model of bone growth

An iterative finite element (FE) modeling approach was used to predict the osseous morphological growth in response to biological and mechanical stimuli (Abaqus 6.13.3, Dassault Systemes). We extend earlier work (Giorgi et al., 2015, 2014) by incorporating realistic 3D geometries in our simulations. Initial geometry for all simulations was defined using an existing micro CT scan of an uninjured neonatal rat (Crouch et al., 2015). The geometry was reduced to include only the glenoid and humeral head regions to improve computational efficiency of the analysis (Fig. 2). Because these neonatal bones are mostly cartilaginous in the region of interest, a cartilage material model was applied, with a Young's modulus of 1.1 MPa and Poisson's ratio of 0.45 (Giorgi et al., 2014). The geometry was meshed using quadratic tetrahedral elements (type C3D10M) with smaller elements near the articulating surface. The mesh had an element size of 0.760 mm^3 for the scapula and 0.890 mm^3 for the humerus in

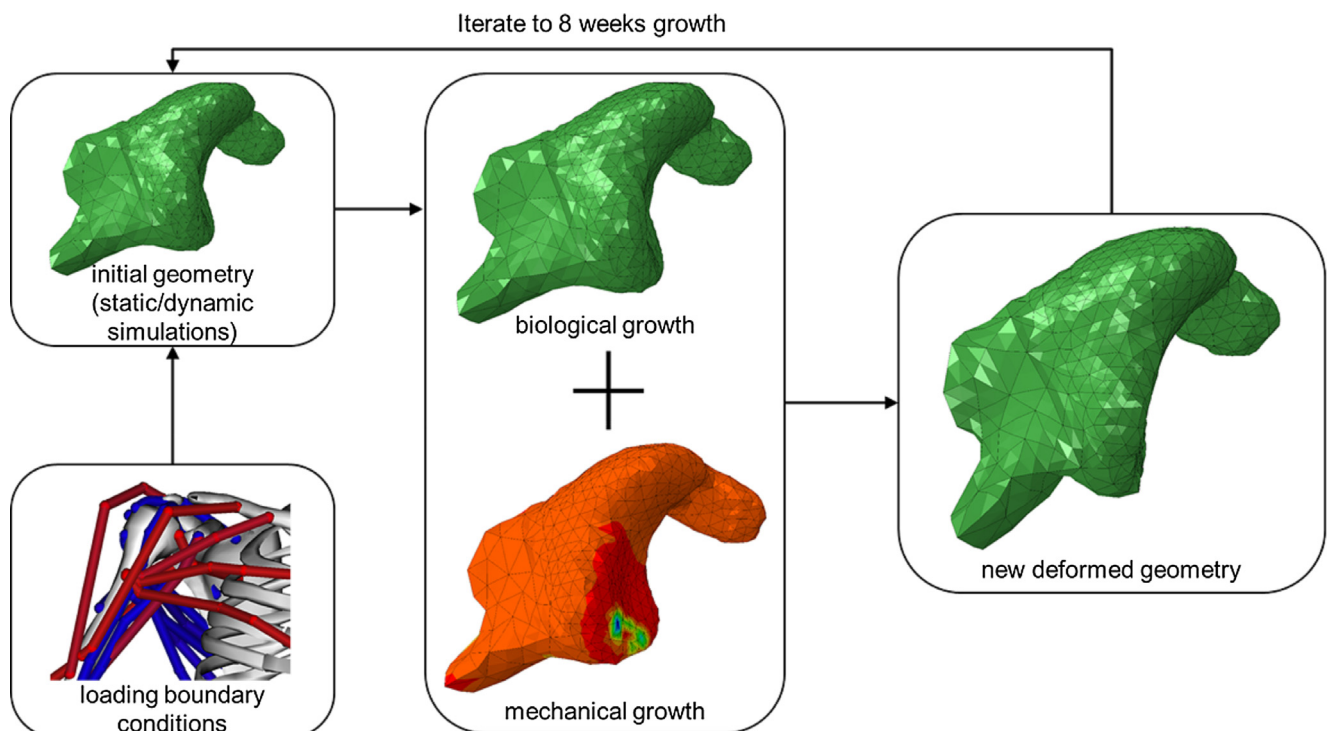


Fig. 1. Iterative computational framework to predict glenohumeral growth. Boundary conditions derived from multibody dynamic modeling of the shoulder musculoskeletal system informed finite element models of biological and mechanical stimulus for bone growth using a thermal expansion analog.

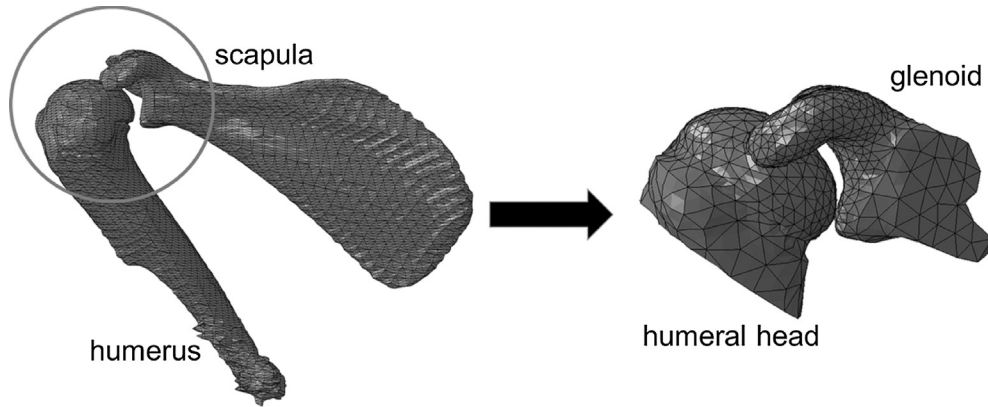


Fig. 2. Initial glenohumeral model geometry. Meshes defining the geometry of a typically developing neonatal rat scapula and humerus derived from microCT were reduced to include only the glenoid and humeral head articulating regions to increase computational efficiency.

the volume away from articulating surface. We performed a convergence study to identify the mesh density needed to converge the peak contact stress in the articulating region under a constant humeral head displacement of 0.23 mm (exceeding all displacements used in the simulations). Near the contact region, we performed simulations with mesh densities determined by increasing the seed number along the circumferential edge of each volume from 10 to 70 in increments of 10, equivalent to element sizes of 1.247–0.178 mm³ on the glenoid and 1.770–0.252 mm³ on the humeral head. The location of the peak stress was monitored, and the magnitude of peak contact stress (Fig. 3) was monitored by normalizing to contact stress predicted with a very fine mesh with a seed number of 120 (element size of 0.103 mm³ on the glenoid and 0.147 mm³ on the humeral head). Mesh densities over 40 seeds resulted in peak stress within 10% of the very fine mesh simulation and no change in peak stress location. Based on this result we used element size of 0.312 mm³ on the glenoid and 0.440 mm³ on the humeral head in the region of contact. The final glenoid mesh contained 6447 elements with 9822 nodes and the final humeral head mesh con-

tained 4730 elements with 7109 nodes. A frictionless impenetrable surface-to-surface contact was defined between the two articulating surfaces.

Biological growth for the humeral head was modeled using a cubic equation (Eq. (1)), relevant to the growth of long bones, that was a function of distance from the growth plate (Heegaard et al., 1999):

$$\dot{\epsilon}_b = C_d = k(0.14 - 0.87\xi + 4.40\xi^2 - 2.66\xi^3) \quad (1)$$

where $\dot{\epsilon}_b$ is the biological growth rate, proportional by constant k to the chondrocyte density C_d ; ξ is the distance of each node along the proximal-distal axis from the distal end of the rudiment. For the analysis, k was defined to be 11,000; the constant determines the contribution of biological growth (Giorgi et al., 2014), and was chosen to maintain the biological growth component as 75–85% of the total growth (Germiller and Goldstein, 1997). Biological growth for the glenoid was defined to be isometric in all directions due to the multiple growth centers present within the region of interest.

Mechanical growth was defined to be proportional to the compressive hydrostatic stress at every node. Stress due to static loads

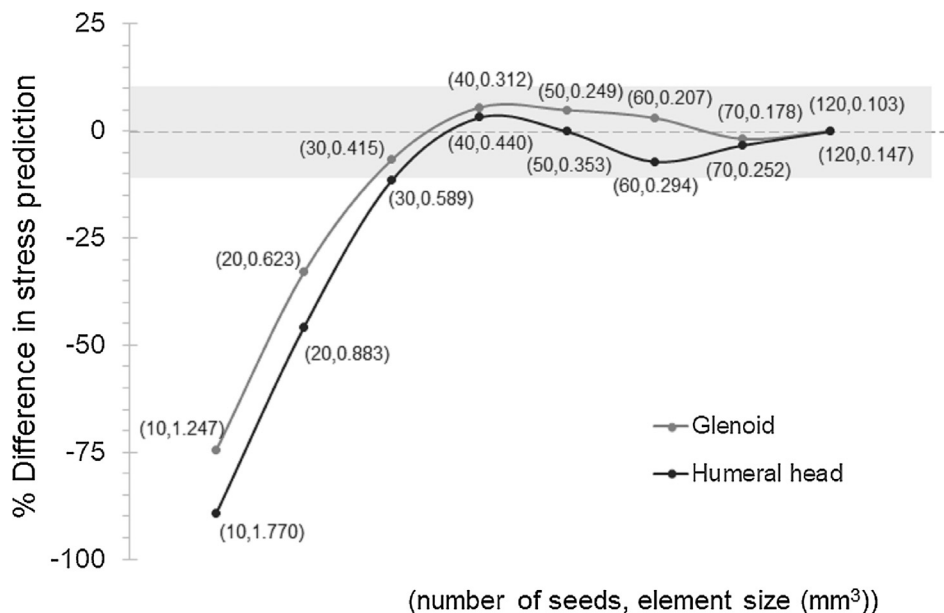


Fig. 3. Mesh convergence for predicted peak contact stresses on the glenoid and humeral head geometries. Meshes created using greater than 40 seeds resulted in peak stress within 10% (shaded region) of peak stresses predicted using a very fine mesh created with 120 seeds for both the humeral head (black) and glenoid (grey). Each simulation point is annotated with the element size mm³ and number of seeds.

restricted the growth while dynamic hydrostatic stress stimulated the growth according to the following equations:

$$\dot{\epsilon}_m = C_d \left(\frac{\sum_{i=1}^N \sigma_{hi}}{N} \right), \text{ for static loads}$$

$$\dot{\epsilon}_m = -C_d \left(\frac{\sum_{i=1}^N \sigma_{hi}}{N} \right), \text{ for dynamic loads} \quad (2)$$

where $\dot{\epsilon}_m$ is the mechanical growth rate, σ_{hi} is the compressive hydrostatic stress, N is the number of iterations per time step to computational convergence, and C_d is the chondrocyte density as determined from the biological calculation above (Eq. (1)).

Thermal expansion was used as an analog to incorporate deformations due to biological and mechanical growth. The growth rates determined from the biological and mechanical governing equations were used to define temperature gradients to identify nodal deformations, and the deformations were summed to create the resultant deformed geometry. Following each timestep, the new geometry was oriented for next cycle of simulation such that the two bodies just touched each other in their deformed state. To do so, we performed a scouting operation to identify the nearest node between the two bodies using an impact filter within an explicit dynamic analysis. The biological and mechanical computations were then repeated. In total, fifteen growth cycles were implemented to model 8 weeks of postnatal growth.

2.2. Musculoskeletal model

Boundary conditions for the loading of the finite element model were obtained from a series of musculoskeletal forward dynamic simulations. Force direction and magnitude calculated in the simulations described below were applied as displacements in the finite element growth model. The resultant joint reaction forces were converted into corresponding displacements using a joint stiffness of 0.7 N/mm (Giorgi et al., 2014).

Joint reaction forces acting at the glenoid were calculated using a musculoskeletal model of the shoulder (Saul et al., 2015) as a foundation, implemented for forward dynamic analysis in OpenSim (Delp et al., 2007) and altered to represent a neonatal rat. Twenty actuators representing muscles crossing the glenohumeral joint were included in the model. Joint forces were scaled using a force reduction factor based on a ratio of average PCSA of subscapularis and infraspinatus in neonatal rats to humans (Swan et al., 2014; Saul et al., 2015).

To capture changes in loading associated with the relative growth of the bones and muscles over time, we calculated loading in two size configurations representing the initial and ending skeletal growth after 8 weeks in a rat (Crouch et al., 2015): with the nominal model and with the skeletal geometry scaled to 1.4 times the starting geometry. To capture the influence of impaired longitudinal growth, we implemented two growth scenarios for the muscles in the model. In the first, both affected and unaffected muscles were allowed to lengthen in proportion to the skeletal growth (unrestricted muscle growth). In the second, only unaffected muscles were permitted to lengthen while affected muscles were constrained to maintain the initial optimal muscle fiber length at the initial and end skeletal sizes (restricted muscle growth). Linear interpolation was used to estimate loading at intervening timepoints.

Three loading conditions were implemented using this approach. First, we implemented a dynamic condition intended to represent an intact shoulder; thus, all muscles were considered unaffected. A cyclic motion in the scapular plane from 0° to 30° elevation was performed. The muscle activations required to per-

form the motion were obtained using a computed muscle control algorithm (Delp et al., 2007; Thelen and Anderson, 2006). Muscle lengths at the end timepoint were permitted to scale with skeletal size. Resulting joint reaction force was applied as a dynamic load in the finite element analysis.

Next, we simulated two static conditions representing BPBI, including muscle paralysis. We simulated denervation of muscles affected by C5–C6 level BPBI (deltoids, biceps long head, biceps short head, subscapularis, supraspinatus, infraspinatus, teres minor and teres major) (Crouch et al., 2014; Cheng et al., 2015; Hogendoorn et al., 2010; Waters et al., 2009) by restricting activation level to 0 (passive contributions only). All unaffected muscles were activating to 30% (Waters et al., 2009; Cheng et al., 2015). We simulated static loading with muscle length allowed to scale with skeletal growth, and again with affected muscles restricted to maintain the initial optimal fiber length. Joint loads were computed with the shoulder in 30° abduction and applied statically in the finite element simulation.

2.3. Analysis

Post simulation, the glenoid surfaces for each simulation were measured to assess glenoid version angle (GVA), glenoid inclination angle (GIA), and the glenoid radius of curvature (GRC). GVA is the angle complementary to the angle between the centerline of the scapula in the transverse plane and the tangent line along the cavity (Fig. 4(a)). GIA is the angle complementary to the angle between the centerline of the spine of the scapula and the tangent line to the rim of the glenoid cavity (Fig. 4(b)). GRC is measured by fitting a circle to the glenoid curvature (Fig. 4(c)). The GVA, GIA, and the GRC predicted from the growth simulations were compared with existing geometry derived from micro CT at the same 8-week timepoint in rats. Specifically, we examined the geometry in an affected limb which had undergone postganglionic neurectomy (restriction in muscle growth) of the C5–C6 nerve roots at 5 days postnatal, and the contralateral typically developing limb (Crouch et al., 2015).

3. Results

Deformations under the dynamic load preserved the GVA, GIA, and GRC present in the initial configuration, with no flatness on the glenoid surface (Fig. 5). Static loading on the joint resulted in higher GVA, GIA, and GRC, with more declined glenoid fossae and prominent flatness on the glenoid. (Fig. 5b). The change in these measures under dynamic loading to -1.2° , -38.2° , and 2.5 mm, respectively was not remarkable compared to the baseline starting point of -1.8° , -38° , and 2.1 mm, respectively. In contrast, these measures increased in magnitude to 5.2° , -48° , and 3.5 mm, respectively, in the static case with unrestricted muscle growth. More severe joint deformations were observed in GIA and GRC in the case of restricted muscle growth with GVA: 3.6° , GIA: -55° , and GRC: 4.0 mm in the same 8 weeks of simulated growth rat bone growth (Fig. 5b and c).

The growth model predictions were consistent with the glenohumeral joint morphology previously reported for rats developing typically and after BPBI (Table 1). The morphology after simulated dynamic loading had similar GVA, GIA, and GRC to the typically developing rat shoulder. For example, predicted GIA (-38.2°) was similar to GIA from experimental data ($-38.4^\circ \pm 3.7$), as were predicted (2.5 mm) and experimental (2.7 mm \pm 0.2) GRC. We compared the static simulation with restricted growth to measurements in rats following postganglionic neurectomy, in which restricted ROM and longitudinal muscle growth have both been reported (Crouch et al., 2015). Both computational and

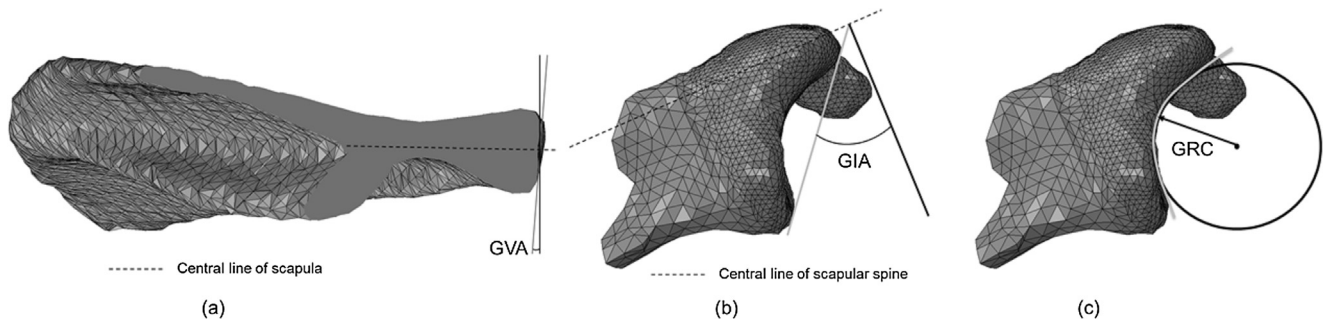


Fig. 4. Bone deformity measures. Glenoid deformity was quantified by measuring (a) GVA, (b) GIA, and (c) GRC. GVA is the angle complementary to the angle between the centerline of the scapula in the transverse plane and the tangent line along the cavity, GIA is the angle complementary to the angle between the centerline of the spine of the scapula and the tangent line to the rim of the glenoid cavity, and GRC is measured by fitting a circle to the glenoid curvature.

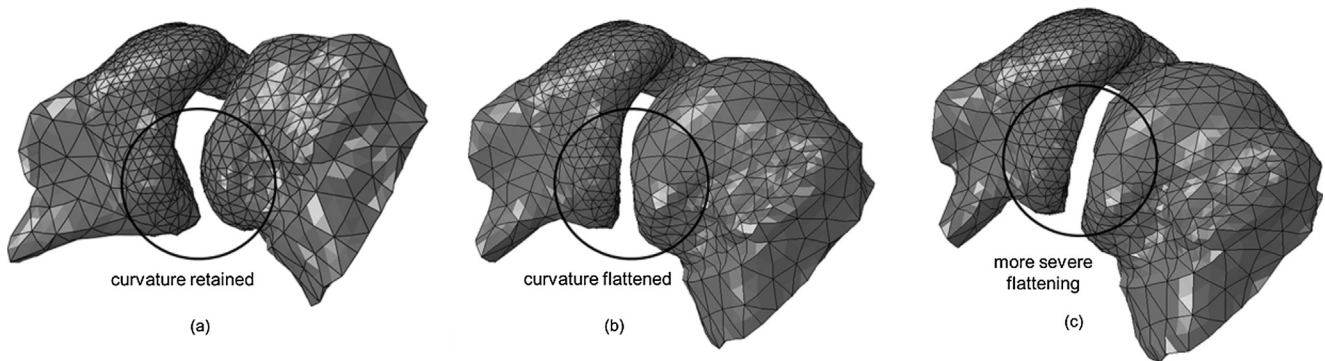


Fig. 5. Glenoid geometry after simulated 8 weeks of growth under (a) dynamic loading and (b) static loading with unrestricted muscle growth, and (c) static loading with restricted muscle growth. The glenoid curvature essential for effective functioning of the joint was retained in dynamic loading, but was flattened and declined under static loading, with more severe changes when muscle growth was restricted.

Table 1
Predicted and experimentally measured glenoid morphology.

	Simulation				Experiment ^a	
	Baseline starting point	Dynamic load	Static: unrestricted muscle growth	Static: restricted muscle growth	Unaffected joint	Postganglionic neurectomy (restricted muscle growth)
GVA (deg)	-1.8	-1.2	5.2	3.6	7.7 ± 4.1	0.2 ± 10.1
GIA (deg)	-38	-38.2	-48	-55	-38.4 ± 3.7	-56.1 ± 16.6
GRC (mm)	2.1	2.5	3.5	4.0	2.7 ± 0.2	5.7 ± 0.37

^a Crouch et al. (2015).

experimental measures displayed more declined and flattened glenoids compared to the baseline condition, with values within the experimentally measured range (GVA: simulation: 3.6°, experiment: 0.2 ± 10.1°; GIA: simulation: -55°, experiment: -56.1° ± 16.6°; GRC: simulation: 4.0 mm, experiment: 5.7 mm ± 3.7). No experimental data is currently available for a BPBI model in rats with reduced contracture or in the absence of restricted growth, with which the simulation results from unrestricted muscle growth could be compared.

4. Discussion

We examined whether and to what extent static joint loading and restricted muscle growth following BPBI influences glenohumeral joint morphogenesis, providing insight into the mechanical underpinnings of formation of joint deformities. The computational analysis predicted that the bone deformities were primarily related to static loads associated with paralysis and disuse. The simulations also showed notable differences in the

bone morphology under restricted and unrestricted muscle growth scenarios, with glenoid deformities being more pronounced with restricted muscle growth. The overall joint shapes predicted from models in which both static loading and restricted longitudinal growth of muscle were included replicated the altered morphology of the glenoid in rats after a postganglionic neurectomy (Crouch et al., 2015), suggesting that altered mechanical loading may account for the altered glenoid morphology after BPBI.

The computational techniques employed here to model joint morphological changes with growth build upon earlier work simulating the mechanical and biological bone development over a cross section (Van Der Meulen et al., 1993), FE bone growth modeling (Heegaard et al., 1999; Giorgi et al., 2014, 2015) and stress predictions over 3D surfaces (Carrero et al., 2011; Shefelbine and Carter, 2004; Roddy et al., 2011). However, the formation of 3D osseous deformities at the shoulder, or the direct effect of muscle abnormalities on osseous deformity that we capture in the current simulations, have not been previously studied.

The simulations predicted osseous changes to the glenohumeral joint characterized by glenoid declination and increased radius of curvature, as validated against existing measurements in rats (Li et al., 2010; Crouch et al., 2015). Analogous declination deformity has been reported in human patients (Pearl and Edgerton, 1998; Sheehan et al., 2014), although retroversion is generally accepted as the most common clinical presentation (Bhardwaj et al., 2013; Eismann et al., 2016; Sibinski et al., 2010). In rat models of BPBI, retroversion is not as pronounced, and variable across animals (Li et al., 2010, 2008), which is reflected in the relatively minor changes to GVA in the current simulations. While osseous deformity has been quantified only in postganglionic conditions in a rat model, evidence in human patients suggests that shoulder osseous and postural deformities may be more severe in postganglionic injury compared to preganglionic injury. Contractures are reported to be significantly more severe following nerve ruptures (postganglionic) compared to nerve root avulsions (preganglionic) (Al-Qattan, 2003), and glenohumeral bone deformities are known to be significantly correlated to the extent of shoulder contracture (Pearl and Edgerton, 1998; Kozin, 2004; Bhardwaj et al., 2013). In prior simulations of joint loading after BPBI using the approach described here for determining the joint loading boundary conditions (Cheng et al., 2015), external rotation ROM was predicted to be greatly reduced when muscle growth was restricted and force components in the compressive and posterior direction, force magnitudes were higher when muscle growth was restricted. In the current study, we extend these results to demonstrate that these altered forces can be directly linked to altered growth patterns that lead to more severe morphological changes under loading conditions that restrict muscle growth. Therefore, the current simulations provide a mechanical explanation for the clinical observation that restricted ROM and contracture correlate with increased osseous deformity.

Limitations to the current study should be considered. A single plane of motion was used for simulation of dynamic conditions; three-dimensional motion would likely contribute to morphological development in other planes. Simulations with dynamic loading did not consider contributions from intermittent static loads. A typically functioning joint would experience a combination of static and dynamic forces governing the overall evolution of the joint (Giorgi et al., 2014). Joint stiffness, which was used to convert joint forces to equivalent displacements for application in the finite element models, was kept constant in all simulations and over time. It is possible that the effective stiffness may vary with condition or time. We estimated the simulated finite element model stiffness for the glenohumeral joint assemblies at the half way and end points of the simulations by measuring the peak deformation at the joint interface obtained when a constant force was applied to the humeral head. Stiffnesses at both timepoints for all static and dynamic simulations were within 10% and 15%, respectively, of the stiffness of the initial geometry. The model accounted for the effect of restriction in longitudinal growth following BPBI (Nikolaou et al., 2011), but not other potential changes to muscle properties. Muscle fibrosis (Nikolaou et al., 2014) and atrophy (Eismann et al., 2015) following BPBI have also been reported. Future studies should explore the contributions of these changes on bone deformation for both preganglionic and postganglionic injuries in which muscle response and patient presentation may differ (Nikolaou et al., 2015). We defined material properties of the cartilage to be linear elastic, isotropic and homogeneous. Although cartilage is a biphasic material (Roddy et al., 2011), we modelled cartilage as a single phase nearly incompressible material (Poisson's ratio 0.49) (Giorgi et al., 2014). Previous studies (Carter and Wong, 2003; Shefelbine and Carter, 2004) have shown that the fluid pressure in biphasic models and hydrostatic stress in single phase models are similar when loaded at 1 Hz, which is approximately the frequency of muscle contraction (Vaal et al.,

2000). In this study, static simulations did not have applied loading at 1 Hz. However, prior work in the simulation of joint morphogenesis using a single phase model were successfully extended to predict bone development under hip dysplasia under both static and dynamic loading (Giorgi et al., 2015, 2014). Additional future work is needed to capture the effects of incorporating the single phase material in this framework when loading occurs under varied loading frequencies. The effect of synovial fluid at the joint does not play a crucial role in defining joint morphology (Giorgi et al., 2014); hence we did not model the synovial fluid interface in our simulations. We used a cartilaginous material model over the entire 8 weeks of growth simulation, however some ossification occurs during this period; future simulations could incorporate evolving material models over time to address this limitation. We modeled isotropic biological growth for the glenoid of the scapula, but there are multiple ossification centers at this stage of development (Nougarolis et al., 2017), and each may have different biological growth rates. Differing growth rates along the glenoid cavity may contribute to the differences observed between predicted and experimental GRC. We examined only changes in the glenoid. We do not report changes to the humeral head, however, the flatness at the humeral head surface due to the injury has been reported in previous studies (Sibinski et al., 2010). The biological growth was held constant across all the simulations, but the nerve injury may affect the biological growth directly. We used a linear interpolation of joint reaction forces over the iteration period, but loading may not change in a linear fashion over time. The loading pattern on the joints was obtained from a scaled musculoskeletal model using the human glenohumeral joint as a foundation; while muscle and joint geometry and osseous morphological response to BPBI is very similar in rat and human shoulders (Norlin et al., 1994), they are not identical. Development of a rat forelimb musculoskeletal model should be pursued to improve representation of muscle and joint forces in future work. The current simulations have been validated for the 8-week time point. However, additional experimental data is needed to validate and refine intermediate time points.

Our iterative model predicted that static loading of the joint is primarily responsible for joint deformation due to BPBI, whereas dynamic loading will result in typical joint growth. The model captured the effects of altered muscle forces due to paralysis and restricted longitudinal growth on the glenoid and predicted that restricted longitudinal results in more severe changes to the glenoid. The computational analyses predicted morphological changes to glenoid that were consistent with experimental data describing glenoid morphology after BPBI in a rat model. This approach offers an avenue to analyze the effects of mechanical and biological growth together and in isolation and can be extended in future work to explore the effects of surgical and other interventions on osseous growth over time.

Conflict of interest statement

The authors have no conflicts to disclose.

Acknowledgments

The research was funded by the National Center for Simulation in Rehabilitation Research (NIH2 P2CHD065690-06) and NIH 1 R21 HD088893-01.

References

- Al-Qattan, 2003. Obstetric brachial plexus palsy associated with breech delivery. *Ann. Plast. Surg.* 51, 257–264 <http://japanknowledge.com/lib/display/?lid=40300SPED510400>.

- Bhardwaj, P., Burgess, T., Sabapathy, S.R., Venkataramani, H., Ilayaraja, V., 2013. Correlation between clinical findings and CT scan parameters for shoulder deformities in birth brachial plexus palsy. *J. Hand Surg.* 38, 1557–1566 <http://www.ncbi.nlm.nih.gov/pubmed/23816519>.
- Brochard, S., Mazingo, J.D., Alter, K.E., Sheehan, F.T., 2016. Three dimensionality of gleno-humeral deformities in obstetrical brachial plexus palsy. *J. Orthop. Res.* 34, 675–682. <https://doi.org/10.1002/jor.23049/abstract>.
- Carriero, A., Jonkers, I., Shefelbine, S.J., 2011. Mechanobiological prediction of proximal femoral deformities in children with cerebral palsy. *Comput. Methods Biomech. Biomed. Eng.* 14, 253–262. <https://doi.org/10.1080/10255841003682505>.
- Carter, D.R., Wong, M., 2003. Modelling cartilage mechanobiology. *Philos. Trans. R. Soc. London. Ser. B: Biol. Sci.* 358, 1461–1471 <http://rstb.royalsocietypublishing.org/content/358/1437/1461.abstract>.
- Cheng, W., Cornwall, R., Crouch, D.L., Li, Z., Saul, K.R., 2015. Contributions of muscle imbalance and impaired growth to postural and osseous shoulder deformity following brachial plexus birth palsy: a computational simulation analysis. *J. Hand Surg.* 40, 1170–1176 <http://www.ncbi.nlm.nih.gov/pubmed/25847723>.
- Crouch, D.L., Hutchinson, I.D., Plate, J.F., Antoniono, J., Gong, H., Cao, G., Li, Z., Saul, K.R., 2015. Biomechanical basis of shoulder osseous deformity and contracture in a rat model of brachial plexus birth palsy. *J. Bone Joint Surg. Am.* 97, 1264–1271 <http://www.ncbi.nlm.nih.gov/pubmed/26246261>.
- Crouch, D.L., Plate, J.F., Li, Z., Saul, K.R., 2014. Computational sensitivity analysis to identify muscles that can mechanically contribute to shoulder deformity following brachial plexus birth palsy. *J. Hand Surg.* 39, 303–311 <http://www.ncbi.nlm.nih.gov/pubmed/24342260>.
- Delp, S.L., Anderson, F.C., Arnold, A.S., Loan, P., Habib, A., John, C.T., Guendelman, E., Thelen, D.G., 2007. Opensim: open-source software to create and analyze dynamic simulations of movement. *IEEE Trans. Biomed. Eng.* 54, 1940–1950 <http://ieeexplore.ieee.org/document/4352056>.
- Eismann, E.A., Laor, T., Cornwall, R., 2016. Three-dimensional magnetic resonance imaging of glenohumeral dysplasia in neonatal brachial plexus palsy. *J. Bone Joint Surg. Am.* 98, 142–151 <http://www.ncbi.nlm.nih.gov/pubmed/26791035>.
- Eismann, E.A., Little, K.J., Laor, T., Cornwall, R., 2015. Glenohumeral abduction contracture in children with unresolved neonatal brachial plexus palsy. *J. Bone Joint Surg. Am.* 97, 112–118 <http://www.ncbi.nlm.nih.gov/pubmed/25609437>.
- Foad, S.L., Mehlman, C.T., Ying, J., 2008. The epidemiology of neonatal brachial plexus palsy in the united states. *J. Bone Joint Surg.* 90, 1258–1264 <http://jbjs.org/article.aspx?articleid=28711>.
- Germiller, J.A., Goldstein, S.A., 1997. Structure and function of embryonic growth plate in the absence of functioning skeletal muscle. *J. Orthopaedic Res.: Official Publ. Orthopaedic Res. Soc.* 15, 362–370 <http://www.ncbi.nlm.nih.gov/pubmed/9246082>.
- Giorgi, M., Carriero, A., Shefelbine, S.J., Nowlan, N.C., 2015. Effects of normal and abnormal loading conditions on morphogenesis of the prenatal hip joint: application to hip dysplasia. *J. Biomech.* 48, 3390–3397 <http://www.sciencedirect.com/science/article/pii/S0021929015003395>.
- Giorgi, M., Carriero, A., Shefelbine, S.J., Nowlan, N.C., 2014. Mechanobiological simulations of prenatal joint morphogenesis. *J. Biomech.* 47, 989–995 <http://www.ncbi.nlm.nih.gov/pubmed/24529755>.
- Heegaard, J.H., Beaupré, G.S., Carter, D.R., 1999. Mechanically modulated cartilage growth may regulate joint surface morphogenesis. *J. Orthop. Res.* 17, 509–517. <https://doi.org/10.1002/jor.1100170408/abstract>.
- Hogendoorn, S., Overvest, Van, Karlijn, L.J., Watt, I., Duijsens, A.H.B., Nelissen, Rob G. H.H., 2010. Structural changes in muscle and glenohumeral joint deformity in neonatal brachial plexus palsy. *J. Bone Joint Surg.* 92, 935–942 <http://jbjs.org/article.aspx?articleid=5973>.
- Kozin, S.H., 2004. Correlation between external rotation of the glenohumeral joint and deformity after brachial plexus birth palsy. *J. Pediatr. Orthop.* 24, 189–193 <http://japanknowledge.com/lib/display?lid=40300SPED510400>.
- Li, Z., Barnwell, J., Tan, J., Koman, A.L., Smith, B.P., 2010. Microcomputed tomography characterization of shoulder osseous deformity after brachial plexus birth palsy: a rat model study. *J. Bone Joint Surg.* 92, 2583–2588 <http://jbjs.org/article.aspx?articleid=5797>.
- Li, Z., Ma, J., Apel, P., Carlson, C.S., Smith, T.L., Koman, L.A., 2008. Brachial plexus birth palsy-associated shoulder deformity: a rat model study. *J. Hand Surg.* 33, 308–312 <http://www.sciencedirect.com/science/article/pii/S0363502307010398>.
- Nikolaou, S., Hu, L., Cornwall, R., 2015. Afferent innervation, muscle spindles, and contractures following neonatal brachial plexus injury in a mouse model. *J. Hand Surg.* 40, 2007 <http://www.ncbi.nlm.nih.gov/pubmed/26319770>.
- Nikolaou, S., Liangjun, H., Tuttle, L.J., Weekley, H., Christopher, W., Lieber, R.L., Cornwall, R., 2014. Contribution of denervated muscle to contractures after neonatal brachial plexus injury: not just muscle fibrosis. *Muscle Nerve* 49, 398–404. <https://doi.org/10.1002/mus.23927/abstract>.
- Nikolaou, S., Peterson, E., Kim, A., Wylie, C., Cornwall, R., 2011. Impaired growth of denervated muscle contributes to contracture formation following neonatal brachial plexus injury. *J. Bone Joint Surg.* 93, 461–470 <http://jbjs.org/article.aspx?articleid=6228>.
- Norlin, R., Hoe-Hansen, C., Oquist, G., Hilderbrand, C., 1994. Shoulder region of the rat: anatomy and fiber composition of some suprascapular nerve branches. *Anatomical Rec.* 239, 332–342.
- Nougarolis, F., Mokrane, F., Sans, N., Rousseau, H., Dedouit, F., Telmon, N., 2017. Bone age estimation based on multislice computed tomography study of the scapula. *Int. J. Legal Med.* 131, 547–558 <https://search.proquest.com/docview/1867560323>.
- Pearl, M.L., Edgerton, B.W., 1998. Glenoid deformity secondary to brachial plexus birth palsy. *J. Bone Joint Surg.* 80, 659–667 <http://jbjs.org/article.aspx?articleid=24019>.
- Roddy, K.A., Prendergast, P.J., Murphy, P., 2011. Mechanical influences on morphogenesis of the knee joint revealed through morphological, molecular and computational analysis of immobilised embryos. *PLoS One* 6, e17526 <http://www.ncbi.nlm.nih.gov/pubmed/21386908>.
- Saul, K.R., Hu, X., Goehler, C.M., Vidt, M.E., Daly, M., Velisar, A., Murray, W.M., 2015. Benchmarking of dynamic simulation predictions in two software platforms using an upper limb musculoskeletal model. *Comput. Methods Biomech. Biomed. Eng.* 18, 1445–1458. <https://doi.org/10.1080/10255842.2014.916698>.
- Sheehan, F.T., Brochard, S., Behnam, A.J., Alter, K.E., 2014. Three-dimensional humeral morphologic alterations and atrophy associated with obstetrical brachial plexus palsy. *J. Shoulder Elbow Surg.* 23, 708–719.
- Shefelbine, S., Carter, D., 2004. Mechanobiological predictions of femoral anteversion in cerebral palsy. *Ann. Biomed. Eng.* 32, 297–305 <http://www.ncbi.nlm.nih.gov/pubmed/15008378>.
- Sibinski, M., Woźniakowski, B., Drobniowski, M., Synder, M., 2010. Secondary glenohumeral joint dysplasia in children with persistent obstetric brachial plexus palsy. *Int. Orthop.* 34, 863–867 <http://www.ncbi.nlm.nih.gov/pubmed/20174796>.
- Swan, M.A., Sato, E., Galatz, L.M., Thomopoulos, S., Ward, S.R., 2014. The effect of age on rat rotator cuff muscle architecture. *J. Shoulder Elbow Surg.* 23, 1786–1791.
- Thelen, D.G., Anderson, F.C., 2006. Using computed muscle control to generate forward dynamic simulations of human walking from experimental data. *J. Biomech.* 39, 1107–1115 <http://www.sciencedirect.com/science/article/pii/S0021929005000990>.
- Vaal, J., Van Soest, A.J., Knoek, Hopkins, B., 2000. Spontaneous kicking behavior in infants: age-related effects of unilateral weighting. *Dev. Psychobiology* 36, 111–122. [https://doi.org/10.1002/\(SICI\)1098-2302\(200003\)36:23.0.CO;2-H/abstract](https://doi.org/10.1002/(SICI)1098-2302(200003)36:23.0.CO;2-H/abstract).
- Van Der Meulen, M.C.H., Beaupré, G.S., Carter, D.R., 1993. Mechanobiologic influences in long bone cross-sectional growth. *Bone* 14, 635–642 <http://www.sciencedirect.com/science/article/pii/S8756328293900850>.
- Waters, P.M., Monica, J.T., Earp, B.E., Zurakowski, D., Bae, D.S., 2009. Correlation of radiographic muscle cross-sectional area with glenohumeral deformity in children with brachial plexus birth palsy. *J. Bone Joint Surg.* 91, 2367–2375 <http://jbjs.org/article.aspx?articleid=28958>.